Quasi-Steady Magnetoplasmadynamic Thruster Performance Database *

E.Y. Choueiri† and J.K. Ziemer‡
Electric Propulsion and Plasma Dynamics Laboratory (EPPDyL)
MAE Dept.
Princeton University
Princeton, New Jersey 08544§

Nomenclature

E Discharge energy
I_b Impulse bit
I_{cgb} Cold gas impulse bit
I_{hb} "Hot" impulse bit
I_{sp} Specific impulse
J Thruster current
m_{cb} Cold gas mass bit
m_b Propellant mass bit
$\dot{m}$ Mass flow rate
m_{eff} Effective mass of thruster-thrust arm assembly
P Power
T Instantaneous thrust
u_{cge} Cold gas exhaust velocity
V Thruster voltage
V_m Voltage of mass pulse waveform at quasi-steady-state plateau
x Position of thrust stand arm

δV Voltage "hash" fluctuations
Δt_h Effective "hot" pulse duration
Δt_m Effective mass pulse duration
$\Delta \dot{x}$ Change in velocity due to impulse
η_I Impulsive efficiency
η_T Thrust efficiency
ζ_{eff} Damping constant of thrust arm motion
$\omega_{n,eff}$ Effective natural frequency of thruster-thrust arm assembly
$< a >$ Arithmetic average of quantity a over the quasi-steady plateau.

Abstract

The performance of a coaxial, gas-fed, self-field, quasi-steady pulsed magnetoplasmadynamic thruster (MPDT) was measured using a swinging gate thrust stand equipped with a laser interferometer and an RF proximity transducer. Careful calibration of the thrust stand, and other diagnostics insured that the measurement errors, barring the effects of fluctuations in the discharge voltage, are well below 2%. The measurements were carried out for various mass flow rates, ranging between .5 and 6 g/s and for four propellant gases: argon, xenon, hydrogen and deuterium. The data set can be interpreted to describe both the performance of steady-state high-power (multi-megawatt) MPDTs and quasi-steady *pulsed* MPDTs that can operate at low spacecraft bus power. The results were curve-fit and compiled into a performance database that is intended as a data source for system or mission analysis as well as for the validation of analytical and numerical models of the MPDT.

1 Introduction

1.1 Status of MPDT Technology

Quasi-steady pulsed operation of self-field magnetoplasmadynamic thrusters (MPDTs) was originally intended[1, 2] as a means of simulating multi-megawatt steady-state thrusters in the laboratory. The need to operate at high instantaneous power stems from the early[3] recognition that MPDTs op-

*Presented at the 34^{th} AIAA Joint Propulsion Conference, Cleveland, OH, July 13-16, 1998. AIAA-98-3472.

†Chief Scientist at EPPDyL. Assistant Professor, Applied Physics Group, MAE Dept. and Associated Faculty at the Dept. of Astrophysical Sciences, Program in Plasma Physics. Senior Member AIAA.

‡Graduate Student, Research Assistant. Presently at NASA-JPL. Member AIAA.

§Research supported by NASA-JPL's program on advanced propulsion.

erate more efficiently with increasing power[1]. Two facts eventually became clear by the late eighties. First, the prospects of MW-level power in space had considerably receded with the continuous lack of evolution in space nuclear power programs. Second, the regime in which MPDTs start to become efficient is also that in which cathode erosion rates tend to be prohibitive. In the past few years, two approaches around these two obstacles have been adopted.

The first approach, followed presently in the US and Russia, is the revival of interest[5] in alkali metal (specifically lithium) MPDTs with multi-channel cathodes. These steady-state thrusters, sometimes called Lorentz Force Accelerators (LFAs) to differentiate them from gas-fed solid-cathode MPDTs, have substantially lower cathode erosion rates[6, 7] with the added benefit of better performance attributed to the low ionization losses of lithium propellant. Although acceptable lifetimes (>5000 hrs) may be within reach (with the addition of barium to the propellant[6]) and 50% efficiencies are accessible at powers as low 100 kW[8, 5] (using applied magnetic fields[2]), there are still no space-based power sources at these levels. Consequently the Lithium LFA is presently of little interest to commercial satellites and more appropriate for more futuristic heavy cargo and piloted planetary exploration missions being studied at NASA[5].

The second approach, followed presently in Japan and Europe, is more suited for near-term applications. It considers the pulsed quasi-steady MPDT as a *low power* propulsion option in itself. In this incarnation, the quasi-steady pulsing (typically a few hundred μs) allows operation at low bus power levels (as low as 1 kW[9]) and may be advantageous for some near-term missions[10]. Although cold cathode erosion still limits the spectrum of missions due to the limit on the total impulse that a single thruster may deliver, schemes for active cathode heating[11] (which may reduce spot-induced erosion) may soon expand this spectrum. Advances in energy storage and valve technologies are essential to improve the prospects of pulsed MPDTs[12]. In 1996 the first flight test of a 1-kW class gas-fed self-field quasi-steady MPDT occurred on the Japanese SFU spacecraft[9]. Successful implementation of this approach to MPDT application hinges on finding solutions to a number of practical problems such as: valve lifetime, mass utilization efficiency, pulse forming network mass, and cathode heater power expenditure.

[1] A major reason for that dependency is the diminution of the anode power loss fraction with increasing power[4].

[2] Applied magnetic fields are typically only needed for efficient operation below 200 kW.

1.2 Motivation for Performance Characterization

System and mission studies in which quasi-steady gas-fed MPDTs are considered or compared to other options need to rely on accurate performance databases in which the key operation parameters are varied parametrically. Similarly, theoretical models and numerical simulations can benefit from such experimental databases for validation and refinement.

Experimental characterization of the performance of quasi-steady gas-fed, self-field MPDTs have been published by Japanese workers in Refs. [13] for H_2, [14] for NH_3, CH_4, Ne, O_2, [15] for He and [16] for Ar, He and NH_3 using various thruster geometries. Similar studies were published by European workers[17].

A compilation of some of the highest thrust efficiencies measured in the past with gas-fed quasi-steady megawatt-level coaxial self-field MPDTs is shown in Table 1.

In the US, the Princeton full-scale benchmark MPDT has been the subject of numerous detailed studies from 1969 to 1996 (see citations in Refs. [18, 19, 20]) resulting in the most extensive characterization (species, densities, temperatures, oscillations, erosion, discharge symmetry, electrode power deposition, etc.) of a single MPDT geometry. In contrast, measured performance characterization of that same thruster is limited to a single database for argon and nitrogen published by Burton et al.[21] in 1983. A more limited thrust characterization of that thruster was also made in Refs. [22] and [23]. The main goal of this paper is to update and extend this database to include low atomic mass propellant such as hydrogen and deuterium and high atomic mass propellant such xenon. Xenon is also interesting for system and mission analysis where integration with xenon ion or Hall thrusters may be an option.

This paper describes the measurements and the resulting performance database, avoiding any speculation, theoretical or otherwise, on the nature of the dependencies. Such theoretical interpretations are published elsewhere[24].

	H_2	N_2	NH_3	CH_4	Ar	Ne	He	O_2
η (%)	55	38	35	33	30	20	20	18
I_s (s)	10000	4000	5700	6000	2300	4000	2000	2500
Reference	[13]	[21]	[14]	[14]	[22]	[14]	[15]	[14]

Table 1: Some of the highest measured efficiencies for the coaxial self-field MPDT with various gaseous propellants.

2 Apparatus

The MPDT used for the experiments is the so-called Princeton full-scale benchmark thruster (FSBT) shown schematically in Fig. (1) where the dimensions are also given. It is the same one used by Burton et al[21] and is described in more detail in that paper. In brief, the cathode is made of thoriated tungsten, the anode is an annular aluminum disk, the backplate insulator is boron nitride and the side insulator is a Pyrex tube. The exterior is insulated with a nylon sleeve. Propellant is injected through a solenoid valve feeding a choked multiple orifice which splits the flow such that 54% of the mass flow rate goes through an annulus around the cathode base and 46% goes through a ring of 12 holes in the backplate located at a radius of 3.8 cm.

The mass flow rate calibration consisted of calibrating the gas flow rate through the choked orifice injection system as a function of the pressure located just upstream of the orifices. This was done by flowing gas, for various mass pulse lengths and plenum pressures into an enclosure of known volume and monitoring the increase in the pressure. The calibration of the mass injection system used in this study is described in detail in the appendix of ref. [23].

The triggers to the mass pulse and the nitrogen switch controlling the discharge circuit are shown in Fig. (2) along with the waveforms for the mass pulse, thruster current and position of thrust stand arm. Sample thruster current and voltage waveforms are shown on an expanded scale in Fig. (3). As seen in that figure, the discharge current is a quasi-steady flat-top current pulse of about 1 ms. The terminal voltage during the pulse is on the order of 100 V and acquires fluctuations, called voltage "hash" for operation above a certain value of $J^2/\dot{m}$. The voltage hash is due to oscillations intrinsic to the discharge and does not result from electromagnetic interference with the diagnostics which are well shielded inside a large Faraday cage. It has been shown[25] that these fluctuations are related to a transition from a

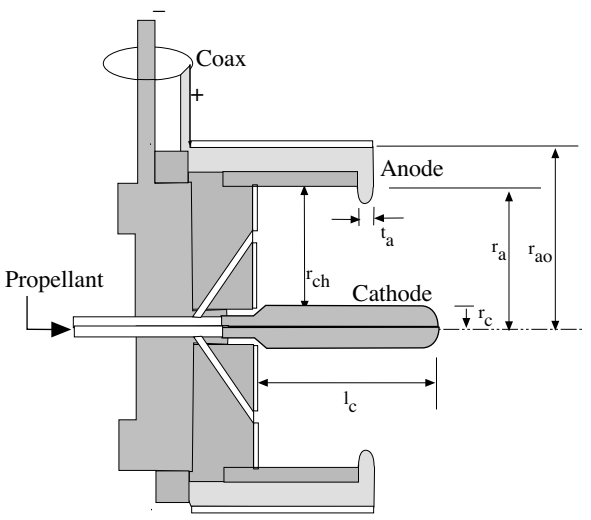

Figure 1: Schematic of the Princeton full-scale benchmark thruster used for the present study. The dimensions are $r_c = 0.95$ cm, $r_a = 5.1$ cm, $r_{ao} = 9.3$ cm, $r_{ch} = 6.4$ cm, $t_a = 0.95$ cm and $l_c = 10$ cm.

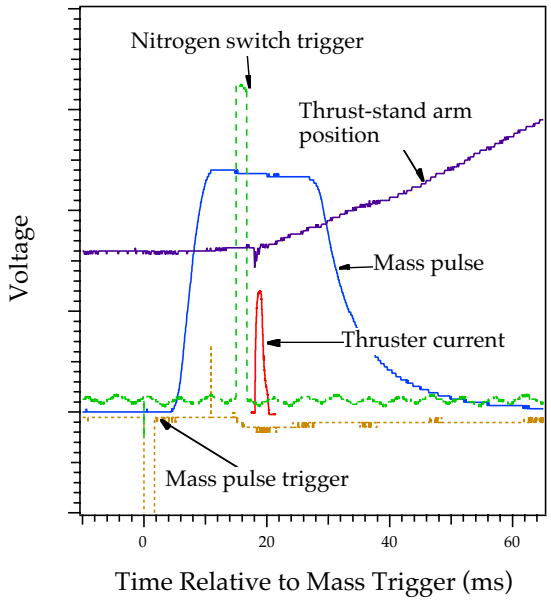

Figure 2: Timing of mass pulse and thruster triggers. Also shown is a sample thrust stand arm position history.

diffusive to a spot mode of current attachment at the anode triggered by a depletion of charge carriers in the anode region.

The current waveform is supplied by a 20-station 12.8 mF L-C pulse forming network (PFN) with an energy storage capability of 120 kJ and can produce rectangular current pulses ranging from .5 to 2 ms and current levels up to 50 kA. All experiments reported here were done at the 1 ms pulse length setting. The 40 mΩ PFN is matched to the 10 mΩ thruster impedance with a series 30 mΩ resistor. A nitrogen gas switch is used to trigger the discharge as shown in Fig. (2). The discharge current is measured with a current transformer and the voltage with a 1000:1 Tektronix probe. The voltage and current are measured at the power leads outside the vacuum tank. These leads connect to the thruster through a low-friction flexural connection and a coaxial lead inside the thrust stand arm. The coaxial lead insures that the current pulse does not interfere with the dynamics of the thrust arm.

The vacuum vessel is a 2 m diameter, 5 m long fiberglass tank with eight optical access ports. A vacuum level on the order of 10^{-5} torr is maintained by two 1.3 m (48-inch) CVC diffusion pumps each with a pumping capability of 120,000 l/s of air. The diffusion pumps are backed by a roots blower (630 l/s) and two mechanical pumps (155 l/s).

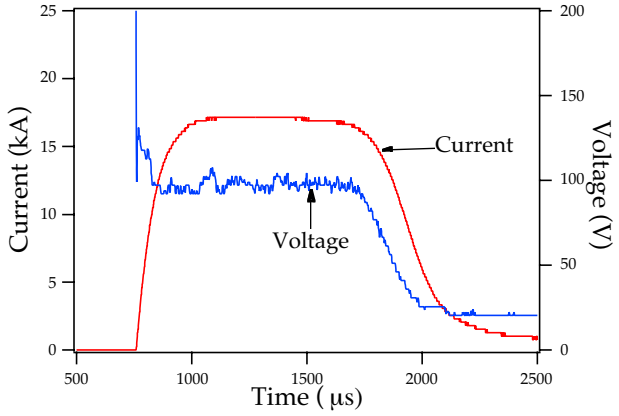

Figure 3: Sample waveforms for thruster current and voltage. Argon at 6 g/s.

2.1 Thrust stand

The thruster assembly weighs about 20 kg and is mounted on a "swinging gate" thrust stand as shown schematically in Fig. (4). The thrust arm is mounted with two flexural pivots. They are series 6016 Bendix Free-Flex Pivots, each with a torsional spring constant of 0.73 N-m/rad. The vertical axis of rotation of the arm can be adjusted to incorporate the force of gravity which can be added or subtracted from the restoring force of the flexural pivots to influence the natural period of the arm. Typical natural periods of the arm are 1-10 seconds. The thrust stand arm is fully described in Ref. [21] and is a modified version of a microthrust stand built by Fairchild Republic[26]. To reduce random mechanical perturbations to the thrust stand system, the entire thrust stand table was mechanically isolated from the tank. This was done by resting the entire structure on rubber supports.

2.2 Thrust Arm Displacement Measurement

The thruster position is measured simultaneously with an RF proximity transducer and an optical interferometric proximeter system (IPS). The two measurements were always in agreement and the more sensitive IPS was relied on for small impulses such as during the cold gas shots.

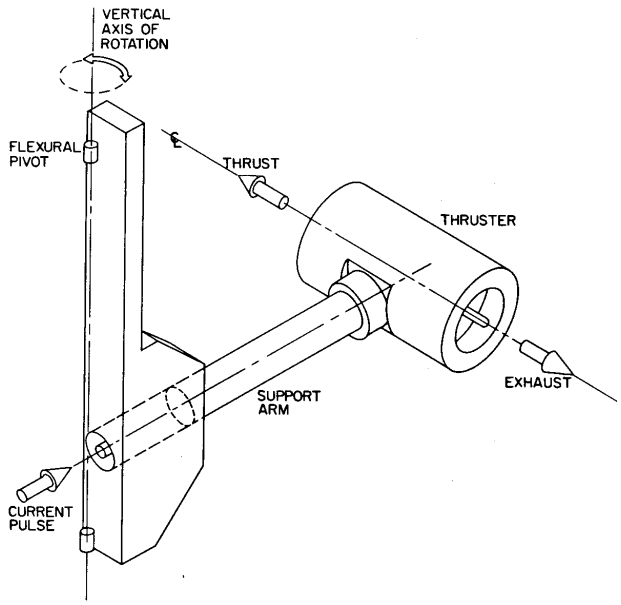

Figure 4: Schematic of "swinging gate" thrust stand.

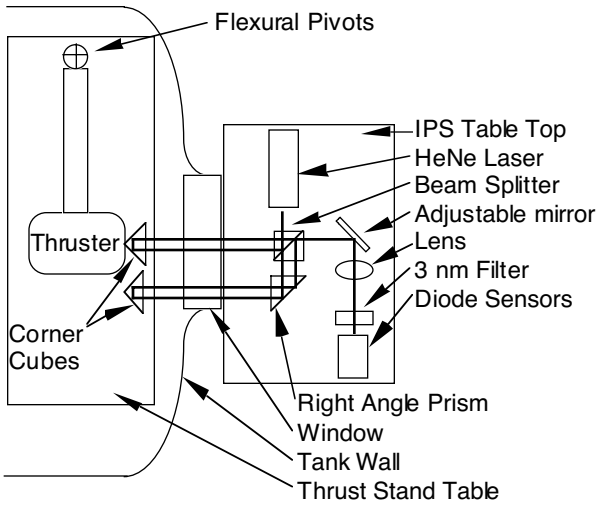

Figure 5: Layout of the interferometric proximeter system (IPS).

The RF proximity transducer is a highly linear 8V/mm Bently-Nevada position transducer. The transducer is located 0.61 m from the hinge axis and measures the displacement of a 4140 steel target mounted on the thruster.

The laser-based IPS was described in detail in ref. [27]. It is mounted on an optical table attached to an access window behind the thruster as shown in Fig. 5. Light emitted from the laser source is split into two beams at the beam splitter. At the end of each path is a corner cube. The two beams are reflected back to the beam splitter and passed through a lens to the diode sensors. The diode sensor output signals are recorded on a computer. Multiple fringes are facilitated by slightly offsetting the two beams at the diode sensors. When the path lengths traversed by the two beams differ by a non-integer multiple of the wavelength of the laser light there is a phase angle difference between them when they are reunited. Superposition of these two waves yields constructive or destructive interference. Analysis of the electronically recorded interference pattern yields a position measurement with a 10 nm accuracy[27].

One corner cube is attached to the thrust stand table and the other to the thruster. A 1 mW Helium-Neon laser (wavelength = 632.8 nm) is used as a light source in the interferometer. Both the beam splitter and the right angle prism are mounted on two adjoined aluminum blocks with separate pitch angle adjustment. Also the beam splitter and right angle prism can each slide sideways to match the horizontal separation of the corner cubes. Both of these adjustments are made until both beams are nearly coincident at the adjustable mirror. The mirror is then used to direct the beams to the diode sensors. Between the mirror and the diodes are a lens and a cylindrical filter with a 1 cm focal length. Finally, there is a 3 nm bandpass filter centered at wavelength 632.8 nm. This prevents virtually all of the stray light from the surroundings from reaching the diode sensors, including light from the plasma discharge. The diode sensors are FDS100 Silicon Photodiodes from Thorlabs Inc. They have a rise time of 10 ns, an active area of 13.7 mm^2, and a spectral response of 350-1100 nm.

2.3 Calibration Pendulum

Deducing the impulse from the position measurement requires the knowledge of the effective mass, m_{eff} of the the thruster-thrust arm assembly. This is done using a calibration pendulum. The calibration impulse is delivered by a 30-cm-long 0.5-kg steel rod that is used as a pendulum. The rod pivots on a teflon pin which was fixed to an aluminum stand. This stand is mounted inside the vacuum tank in front of the thruster and strikes the thruster while

the vacuum tank is exposed to atmosphere. An electromagnet is also mounted on the pendulum stand so that the pendulum can be cocked and then released remotely. The force transducer is a model 208A02 Force Transducer from Piezotronics and was attached to the end of the pendulum which strikes the thruster. The operating range is from 0-400 N. A quantification of the calibration error is given in ref. [27]. The calibration method, described in the next subsection, yielded a value of 15.71 ± 0.27 kg for m_{eff}.

2.4 Thrust Measurement Method

The thrust measurement method has been described in ref. [27] in detail. We summarize here the essence of the method.

If the motion of the thruster-thrust stand assembly during a pulse is characterized by x, the applied impulse bit (I_{bit}) will force the response[28]

$$x(t) = e^{-\zeta_{eff}\omega_{n,eff}t}\frac{I_{bit}/m_{eff}}{\omega_{n,eff}\sqrt{1-\zeta^2}}\sin\left(\sqrt{1-\zeta^2}\omega_{n,eff}t\right). \quad (1)$$

The duration of the impulse must be much less then the natural period of the thrust stand for Eq. (1) to be valid.

More than 20 calibration trials are made at different cocking angles using the calibration pendulum described above. The resulting $x(t)$ traces (obtained with either the IPS or the RF proximity transducer) are fit using Eq. (1). Since I_b is measured by the force transducer this allows inferring $\omega_{n,eff}$, ζ and m_{eff} with high accuracy (the small fit errors are retained and propagated through the overall error analysis). Note that $x(t)$ after an impulse is not a perfect straight line but rather a sine wave.

Following a "hot" pulse, a relatively small portion (<50 ms) of the measured $x(t)$ trace, centered at a time, t^* after the mass pulse is over, is fit with a straight line and the resulting slope represents the approximate velocity at that point in time. Since $x(t)$ after an impulse is not a perfect straight line but rather a sine wave, this estimate is refined by using the derivative of Eq. (1) analytically, with the previously measured values of $\omega_{n,eff}$, ζ and m_{eff} to arrive at a refined value of the velocity velocity $\dot{x}$ at t^*. Since the arm always starts from rest, this gives the total change in velocity $\Delta\dot{x}$. The impulse is then obtained from

$$I_{bit} = m_{eff}\Delta\dot{x}. \quad (2)$$

A sample experiment yields a $\Delta\dot{x}$ of 5.79 mm/s. From Eq. 2 and $m_{eff} = 15.71 \pm 0.27$ kg, the delivered impulse is $I_{bit} = 15.71$ kg $\times$ 5.79 mm/s $= 0.091 \pm 0.0016$ N-s where the error estimate contains all the errors associated with the measurements and fits.

3 Data Reduction Algorithm

The procedure followed to acquire and reduce the data is as follows.

1. For a given mass flow rate, a series of cold gas experiments are done during which the position of the thrust arm and the mass pulse are both recorded digitally.

   (a) The mass pulse is recorded with a pressure transducer in the plenum and, as shown in Fig. (2), lasts for about 40 ms. The arithmetic average of the mass pulse plateau during the 8 ms immediately preceding the discharge (in order to avoid EMI contaminated signals) is calculated . Such quasi-steady plateau averages are denoted by <>. The value of this averaged plateau, in volts, is $< V_m >$. An effective time, Δt_m for the mass pulse is obtained from

   $$\Delta t_m = \frac{\int V_m(t)dt}{< V_m >}, \quad (3)$$

   where $V_m(t)$ is the mass pulse waveform (in Volts) shown in Fig. (2).

   (b) The "cold" gas mass bit m_{cb} is then calculated from

   $$m_{cb} = \dot{m}\Delta t_m. \quad (4)$$

   (c) A line fit is made to a 50 ms portion of the recorded position-vs-time signal (of either the IPS or the RF proximity transducer) starting at a time equal to $\Delta t_m + 5ms$ from the time the mass pulse was triggered. This gives the initial estimate of the arm velocity at a time t^* centered in that time segment. This value is then refined taking into account the sinusoidal curvature of the response represented by Eq. (1) as described in Section 2.4. This yields $\Delta\dot{x}$.

   (d) The cold gas impulse bit is subsequently calculated from

   $$I_{cgb} = m_{eff}\Delta\dot{x}. \quad (5)$$

(e) The cold gas exhaust velocity u_{cge} is then calculated from $u_{cge} = I_{cgb}/m_b$.

2. The thruster is then fired at the same mass flow rate used for the cold gas characterization and the waveforms for discharge current, voltage and thruster position are recorded as in the samples shown in Figs. (2) and (3).

   (a) A plateau value for the current pulse is obtained by averaging a 200 μs portion of the data taken 700 μs after breakdown. This delay is to insure that the averaging is done in the quasi-steady portion of the discharge. As we did for the cold gas case, this average value of the current plateau $< J >$ is then used to obtain an effective "hot" pulse duration Δt_h from the following integral

$$\Delta t_h = \frac{\int J^2(t)dt}{< J >^2}, \tag{6}$$

   where we have used the square of the current in the averaging due to the well-known dependence of the thrust on J^2[24]. This time interval, in turn, yields the mass bit for the "hot" pulse, $m_b = \dot{m}\Delta t_h$.

   (b) The thruster position history (from the IPS or the proximity transducer) is analyzed the same way as was done in 1.c above for the cold gas case. This yields the "hot" impulse bit I_{hb}.

   (c) The final impulse bit is calculated from the following expression

$$I_b = I_{hb} - (\Delta t_m - \Delta t_h)\,\dot{m}u_{cge} \tag{7}$$

   which subtracts the impulse due to the cold gas but leaves in the small contribution of the cold gas, *during* the discharge.

3. The voltage "hash" δV is calculated as the standard deviation of the average of a portion of the voltage waveform that corresponds to the portion of the flat-top current waveform considered above.

4. The following expressions are then used to evaluate the performance parameters

$$\text{Quasi-steady Thrust:} \quad T = \frac{I_b}{\Delta t_h} \tag{8}$$

$$\text{Specific Impulse:} \quad I_{sp} = T/(\dot{m}g_0) \tag{9}$$

$$\text{Input Power:} \quad P = VJ \tag{10}$$

$$\text{Discharge Energy:} \quad E = \int P\,dt \tag{11}$$

$$\text{Thrust Efficiency:} \quad \eta_T = \frac{T^2}{2\dot{m}P} \tag{12}$$

$$\text{Impulsive Efficiency:} \quad \eta_I = \frac{I_b^2}{2m_bE} \tag{13}$$

5. The performance database is compiled by repeating the above procedures after varying the discharge current, the mass flow rate or the type of propellant.

4 Final Performance Database and Conclusions

Following the procedures outlined above, a performance database for argon at $\dot{m} = 1, 3$ and 6 g/s, xenon at 3 and 6 g/s, hydrogen at .5 and 1 g/s and deuterium at 1 g/s were obtained. The data are shown in Figs. 7 to 12. Each data point represents the average of 5 measurements at the same operating conditions. For each gas, a series of four scatter plots including error bars were produced for the following dependencies: $T - J$, $V - J$, $\eta_T - I_{sp}$ and $\eta_I - E$.

Fourth-order polynomial curve fits were carried for each of the data sets and four line plots corresponding to each of the four scatter plots were produced. In order the keep the line plots clear, the error bars were not added. The error bars can be easily seen in the corresponding scatter plots which retain the same scale as the line plots. In order to facilitate the use of this database by other studies, the coefficients for the curve fits are compiled in Table 2.

The major source for the error bars is the voltage hash which can easily exceed 10% above a critical current value of $J^2/\dot{m}$ that depends on the propellant. The second major source of the error bars is the scatter in the data taken at the same conditions. The repeatability of the thruster also suffers with increasing current. All other sources of error do not contribute more than 2% to the error bars.

It is interesting to note from the data (e.g. comparing the bottom panels of Fig. (7)) that the impulsive efficiency, η_I can exceed the thrust efficiency η_T for the same operating conditions. This happens especially at low mass flow rates (or low mass bits). To understand the reason for this difference we compare the definitions of these two efficiencies given in Eqs. (12) and (13) and find that η_I can exceed η_T

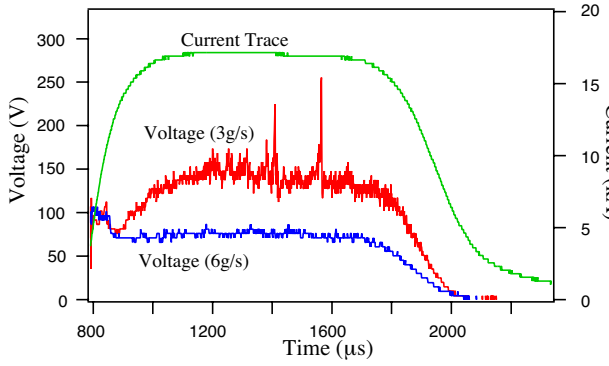

Figure 6: Typical voltage traces showing initial transients and the effects of decreasing mass flow rate on the shape of the voltage waveform. Both traces are for the same current waveform which is also shown.

when the following inequality holds

$$\int J(t)V(t)\,dt \;<\; P\frac{\int J^2\,dt}{< J >^2}. \qquad (14)$$

Since $P \equiv < J >< V >$ the above can be restated as

$$\int J(t)V(t)\,dt \;<\; \frac{\int J^2\,dt}{< J >} < V > . \qquad (15)$$

We have observed in all the cases we studied that the voltage after breakdown initially drops to a certain value that has a far weaker dependence on the total current and mass flow rate than the J and $\dot{m}$ dependencies of the quasi-steady average voltage $< V >$ (which, due to the dominance of the back emf, scales with $J^3/\dot{m}$ at high enough values of $J^2/\dot{m}$. See, ref. [29] for instance.) Consequently, for the same current waveform, the voltage will have to rise from that value to its quasi-steady plateau which is higher with decreasing mass flow rate due to the $1/\dot{m}$ dependence of the back emf voltage. Therefore, with decreasing $\dot{m}$ (and fixed $J(t)$) an increasing portion of the voltage trace is below the average voltage on the quasi-steady plateau $< V >$ and the inequality in Eq. (15) becomes increasingly satisfied. This effect is illustrated with the typical traces shown in Fig. (6) which show the intial transients and the effects of decreasing $\dot{m}$ on the shape of the voltage waveform.

The two efficiencies, η_I and η_T, do not generally differ by more than 10% in the present database. Since the difference between these two efficiencies is due to a transient effect that occurs at the beginning of the pulse, it should be expected that the two efficiencies converge as the pulse length is increased i.e. the quasi-steady plateau is extended. Since this effect is intrinsic to the pulsed operation of the MPDT, it is informative to distinguish between these two efficiencies. Of course, if the voltage and current pulses are perfectly rectangular this difference would also vanish.

Although there have been many studies and much speculation on the level of erosion associated with a particular level of voltage hash, we refrain from speculating, in this experimental study, on the extent to which the high-current portion of the database is affected by not taking into account the eroded mass. While there are some empirical indications[30, 31, 32] that exceeding 10% voltage hash can lead to significant mass addition through erosion, it must be cautioned that these thresholds were formulated for operation with argon only and should not, *a priori* be extended to operation with other gases.

In combination with a wide set of previously published experimental data characterizing the plasma inside the FSBT, this performance database provides the most complete picture to date of a single MPDT configuration operated with various propellants. The final database is intended to be useful for future mission analysis studies and numerical or analytical thruster modeling efforts.

Acknowledgments. This work was supported by grants from the Advanced Propulsion Group at NASA-JPL and the Department of Energy, Program in Plasma Science.

References

[1] D.E.T.F. Ashby, L. Liebing, A.V. Larson, and T.J. Gooding. Quasi-steady-state plasma acceleration. *AIAA Journal*, 4(5):831–835, 1966.

[2] K.E. Clark and R.G. Jahn. Quasi-steady plasma acceleration. *AIAA Journal*, 8:216–220, 1970.

[3] V. M. Nerheim and A. J. Kelly. A critical review of the magnetoplasmadynamic (MPD) thrustor for space applications. Technical Report 32-1196, NASA-JPL, JPL, CIT, Pasadena, CA, USA, 1968.

[4] A.J. Saber. *Anode Power in a Quasi-Steady MPD Thruster*. PhD thesis, Princeton University, Princeton, NJ, USA, 1974.

[5] S. Leifer. Overview of nasa's advanced propulsion activities. In 34^{th} *Joint Propulsion Conference*, Cleveland, OH, USA, 1998. AIAA-98-3183.

[6] V.P. Ageyev and V.G. Ostrovsky. High-current stationary plasma accelerator of high power. In 23^{rd} *International Electric Propulsion Conference*, Seattle, WA, USA, 1993. IEPC-93-117.

[7] J.E. Polk and T.J. Pivirotto. Alkali metal propellants for MPD thrusters. In *AIAA/NASA/OAI Conf. on Advanced SEI Technologies*, Cleveland, Ohio, 1991. AIAA-91-3572.

[8] V. Kim, V. Tikhonov, and S. Semenikhin. Fourth quarterly (final) report to NASA-JPL: 100-150 kw lithium thruster research. Technical Report Contract NASW-4851, RIAME, MAI, Moscow, Russia, April 1997.

[9] K. Toki, Y. Shimuzu, and K. Kuriki. Electric propulsion experiment (EPEX) of a repetitively pulsed MPD thruster system onboard Space Flyer Unit (SFU). In 25^{th} *International Electric Propulsion Conference*, Cleveland, OH, USA, 1997. IEPC-97-120.

[10] E. Y. Choueiri, A. J. Kelly, and R. G. Jahn. Mass savings domain of plasma propulsion for LEO to GEO transfer. *Journal of Spacecraft and Rockets*, 30(6):749–754, 1993.

[11] F. Paganucci, P. Rosssetti, and M. Anderenucci. Optimization of the cathode heating technique in a pulsed MPD thruster. In 34^{th} *Joint Propulsion Conference*, Cleveland, OH, USA, 1998. AIAA-98-3471.

[12] R.M. Myers. Electromagnetic propulsion for spacecraft. 1993. AIAA-93-1086.

[13] H. Tahara, K. Kagaya, and T. Yoshikawa. Hybrid MPD thruster with axial and cusp magnetic fields. In 20^{th} *International Electric Propulsion Conference*, Garmisch-Partenkirchen, W. Germany, 1988. AIAA-88-058.

[14] K. Uematsu, S. Morimoto, and K. Kuriki. MPD thruster performance with various propellants. *Journal of Spacecraft and Rockets*, 22(4):412–416, 1985.

[15] T. Yoshikawa, Y. Kagaya, and K. Kuriki. Thrust and efficiency of the K-III MPD thruster. *Journal of Spacecraft and Rockets*, 21(5):481–487, 1984.

[16] T. Yoshikawa, Y. Kagaya, Y. yokoi, and H. Tahara. Performance characteristics of quasi-steady mpd thrusters. In 17^{th} *International Electric Propulsion Conference*, Tokyo, Japan, 1984. IEPC-84-58.

[17] F. Paganucci and M. Anderenucci. MPD thruster performance using pure gases and mixtures as propellant. In 31^{st} *Joint Propulsion Conference*, San Diego, CA, USA, 1995. AIAA-95-2675.

[18] E.Y. Choueiri. *Electron-Ion Streaming Instabilities of an Electromagnetically Accelerated Plasma*. PhD thesis, Princeton University, Princeton, NJ, USA, 1991.

[19] K.D. Diamant. *The Anode Fall in a High Power Pulsed MPD Thruster*. PhD thesis, Princeton University, Princeton, NJ, USA, 1996.

[20] J. E. Polk. *Mechanisms of Cathode Erosion in Plasma Thrusters*. PhD thesis, Princeton University, Princeton, NJ, USA, 1995.

[21] R.L. Burton, K.E. Clark, and R.G. Jahn. Measured performance of a multi-megawatt MPD thruster. *Journal of Spacecraft and Rockets*, 20(3):299–304, 1983.

[22] M. Wolff, A.J. Kelly, and R.G. Jahn. A high performance magnetoplasmadynamic thruster. In 17^{th} *International Electric Propulsion Conference*, Tokyo, Japan, 1984. IEPC-84-32.

[23] J.H. Gilland. The effect of geometrical scale upon MPD thruster behavior. Master's thesis, Princeton University, Princeton, NJ, USA, 1988.

[24] E. Y. Choueiri. The scaling of thrust in self-field MPD thrusters. *Journal of Propulsion and Power*, 14(5):744–753, 1998.

[25] K.D. Diamant, E.Y. Choueiri, and R.G. Jahn. The role of spot mode transition in the anode fall of pulsed MPD thrusters. *Journal of Propulsion and Power*, 14(6):1036–1042, 1998.

[26] Operating instructions for plasma engine microthruster stand. Technical Report RAC 2392-1, PCD-TR-65-1, Republic Aviation Corporation, January 1965.

[27] E.A. Cubbin, J. Ziemer, and E.Y. Choueiri. Laser interferometric measurements of impulsive thrust. *Review of Scientific Instruments*, 68(6):2339–2346, 1997.

[28] W.T. Thomson. *Theory of Vibrations with Applications*. Prentice-Hall, Englewood Cliffs, NJ, 1993.

[29] L.K. Rudolph. *The MPD Thruster Onset Current Performance Limitation*. PhD thesis, Princeton University, Princeton, NJ, USA, 1981.

[30] L.K. Rudolph, R.G. Jahn, K.E. Clark, and W.F. von Jaskowsky. Onset phenomena in self-field MPD arcjets. In 13^{th} *International Electric Propulsion Conference*, San Diego, CA, 1978. AIAA-78-653.

[31] R. A. Rowe. Ablation of an MPD thruster. Master's thesis, Princeton University, Princeton, NJ, USA, 1981.

[32] D.D. Ho. Erosion studies in an MPD thruster. Master's thesis, Princeton University, Princeton, NJ, USA, 1981.

		$\dot{m}$	a_1	a_2	a_3	a_4	a_5
Ar	T vs J	1	377.98	-0.18079	3.1921e-05	-2.4151e-09	6.7129e-14
		3	750.21	-0.20133	2.0341e-05	-8.8935e-10	1.4599e-14
		6	273.09	-0.057856	4.6962e-06	-1.5357e-10	1.98e-15
	V vs J	1	3225.4	-1.5769	0.0002855	-2.2072e-08	6.2345e-13
		3	2494.3	-0.63077	6.1034e-05	-2.6138e-09	4.3146e-14
		6	-1412	0.38213	-3.6094e-05	1.4756e-09	-2.155e-14
	η_T vs I_{sp}	1	0.13432	-0.00022441	2.3114e-07	-8.4278e-11	1.0756e-14
		3	-0.36688	0.00098812	-6.5927e-07	1.9143e-10	-2.0134e-14
		6	0.005163	0.00011413	1.5326e-07	-1.5329e-10	3.812e-14
	η_I vs E	1	0.11766	-0.00020402	2.5809e-07	-1.093e-10	1.5592e-14
		3	-0.037394	0.00022161	-8.0438e-08	1.2476e-11	-6.799e-16
		6	0.095522	-0.00012457	1.505e-07	-4.55e-11	4.3276e-15
Xe	T vs J	3	-731.65	0.26801	-3.5734e-05	2.0942e-09	-4.4838e-14
		6	-133.15	0.046925	-5.3777e-06	2.6879e-10	-4.5162e-15
	V vs J	3	-6137.2	2.3141	-0.0003155	1.8667e-08	-4.0069e-13
		6	323.86	-0.11658	1.7642e-05	-1.0877e-09	2.4557e-14
	η_T vs I_{sp}	3	-0.038003	0.0002198	-9.5391e-08	-2.2799e-11	1.6098e-14
		6	0.033353	-1.2505e-05	2.0121e-07	-1.4834e-10	2.5677e-14
	η_I vs E	3	-0.048114	0.0001767	-8.5315e-08	1.8298e-11	-1.4336e-15
		6	0.038654	-1.7625e-05	3.892e-08	-1.062e-11	8.2645e-16
H_2	T vs J	.5	-33.736	0.012505	-1.0358e-06	4.4643e-11	-4.8564e-16
		1	-53.66	0.021356	-2.2907e-06	1.2143e-10	-2.0681e-15
	V vs J	.5	498.63	-0.15534	2.8127e-05	-1.8256e-09	4.1344e-14
		1	-57.968	0.077804	-6.4875e-06	3.2688e-10	-5.906e-15
	η_T vs I_{sp}	.5	-0.11854	0.00013362	-2.0091e-08	1.5514e-12	-4.0884e-17
		1	-0.027978	9.6812e-05	-1.8296e-08	2.079e-12	-7.6783e-17
	η_I vs E	.5	-0.1579	0.00024051	-5.4362e-08	5.5818e-12	-1.9217e-16
		1	-0.04706	0.00011432	-2.4302e-08	2.4652e-12	-7.9769e-17
D_2	T vs J	1	-9.0614	0.0036086	8.8895e-09	-4.6713e-12	3.3707e-16
	V vs J	1	42.9	0.0154	1.94e-06	1.02e-10	1.92e-15
	η_T vs I_{sp}	1	-0.0032142	7.0845e-05	-8.2522e-09	9.3289e-13	-3.4625e-17
	η_I vs E	1	-0.011218	9.3084e-05	-1.7907e-08	2.154e-12	-8.2666e-17

Table 2: Coefficients for fourth-order polynomial curve fits of the measured performance database. The curve fits are only valid for the range of parameters shown in the corresponding plot.

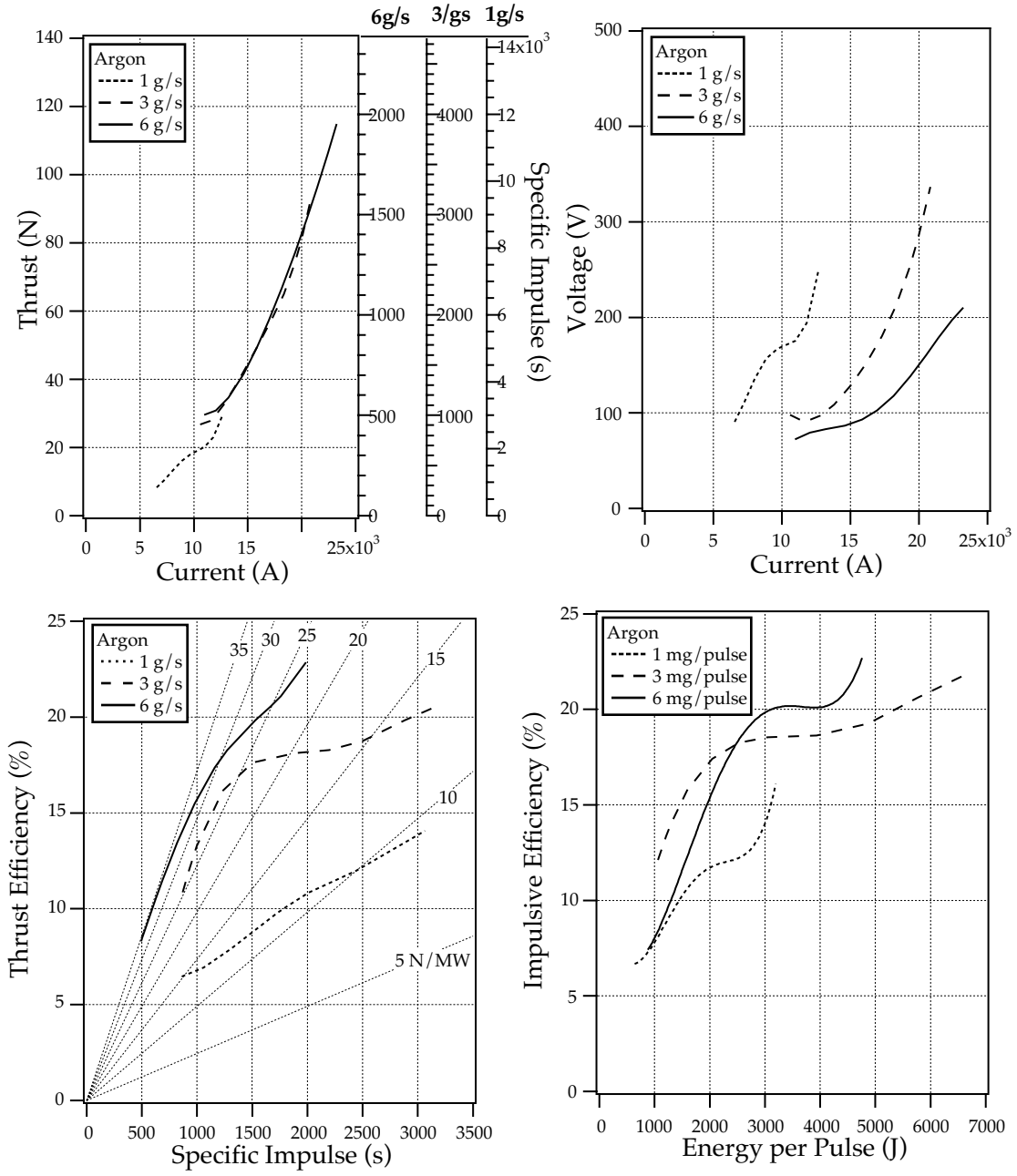

Figure 7: Performance database for argon. The corresponding error bars can be obtained from the scatter plots in Fig. (8).

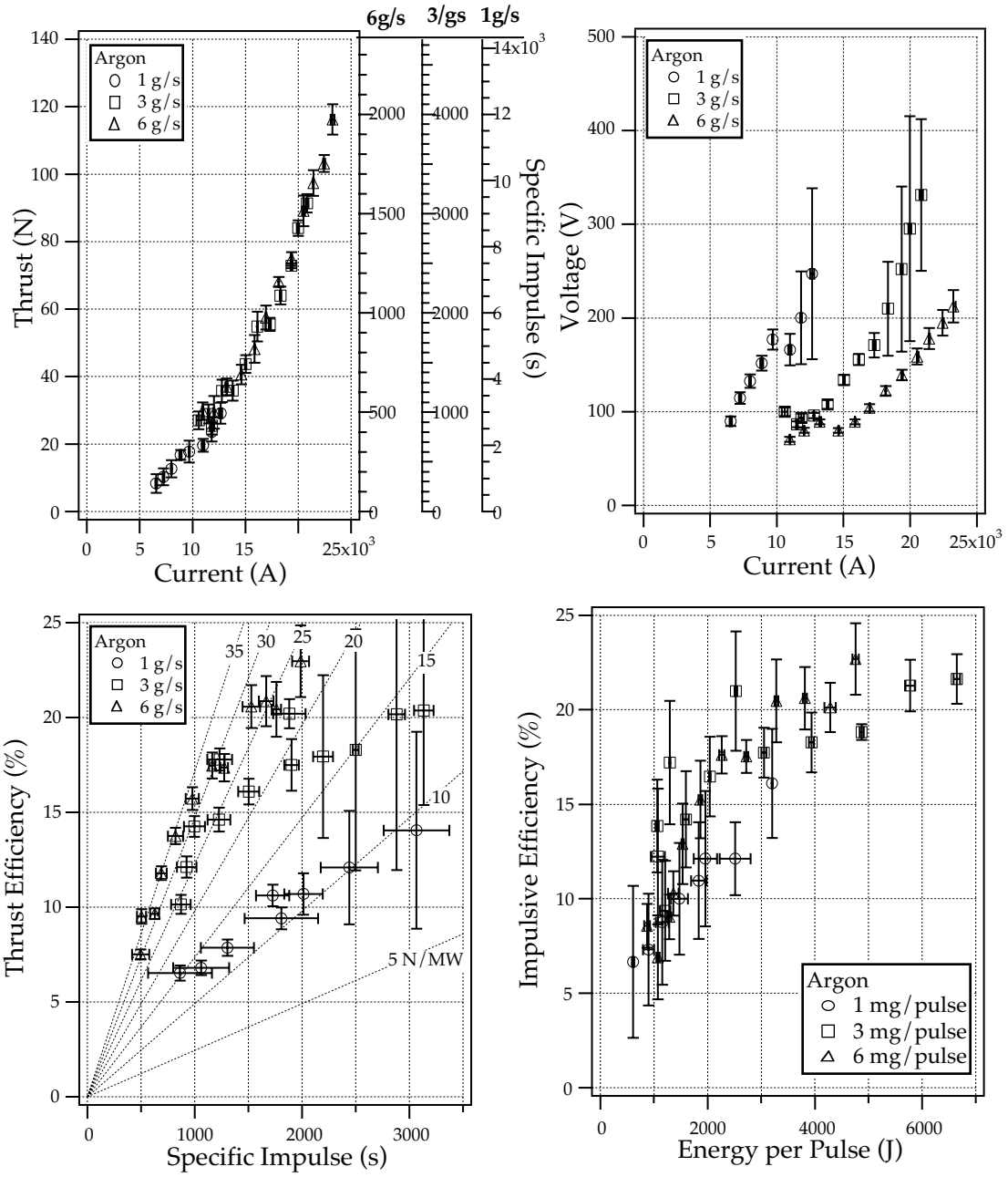

Figure 8: Performance database for argon.

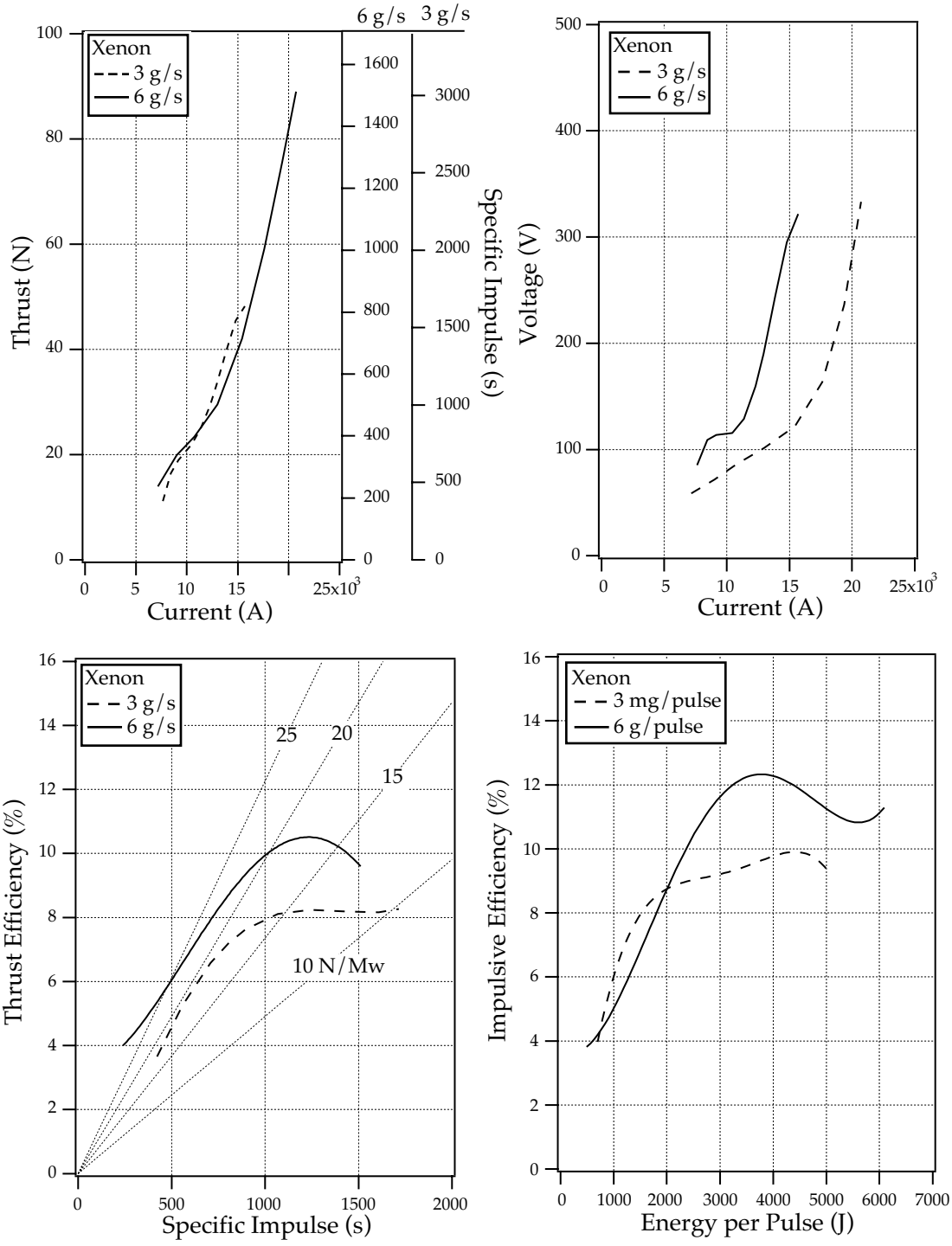

Figure 9: Performance database for xenon. The corresponding error bars can be obtained from the scatter plots in Fig. (10).

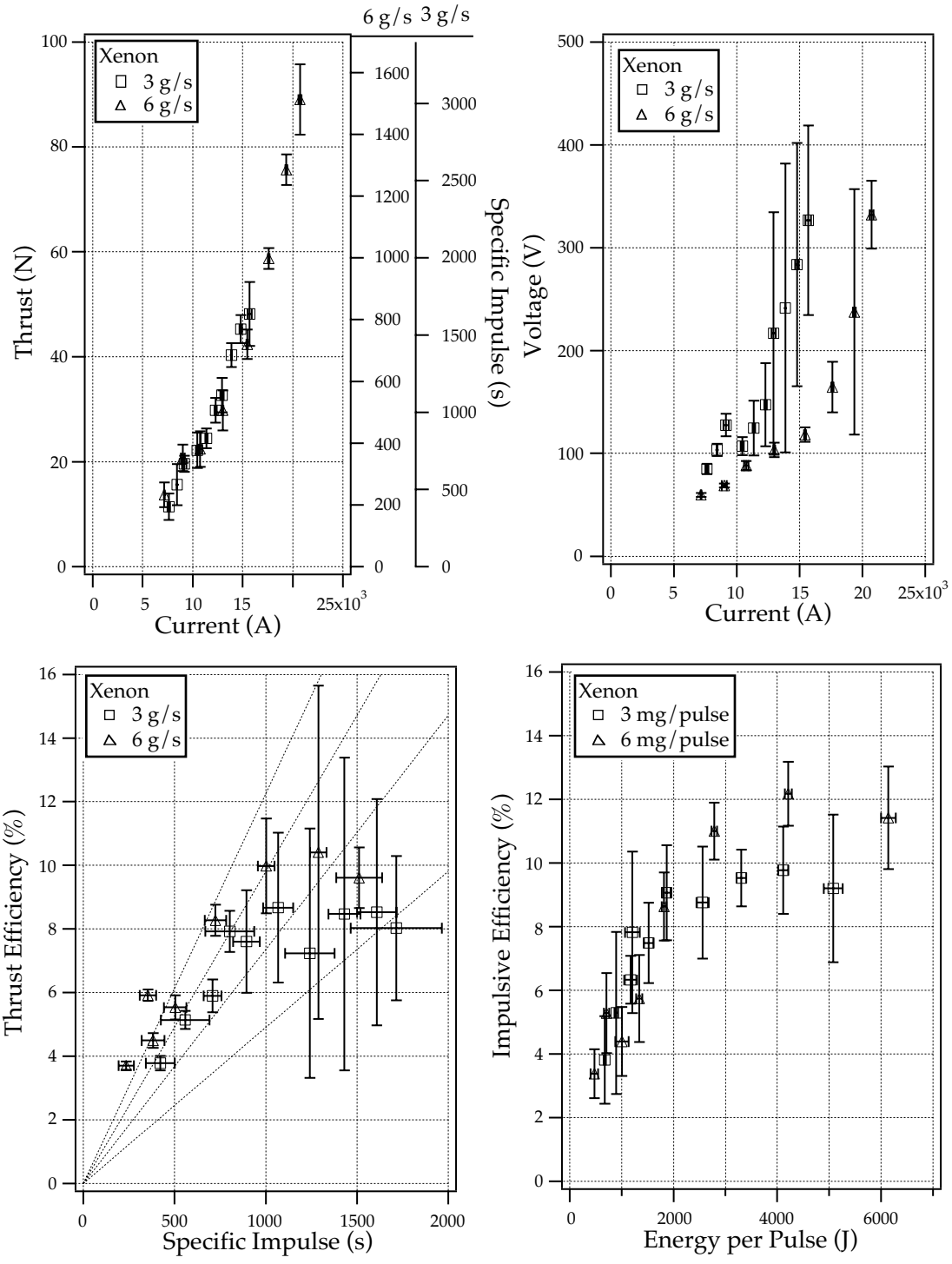

Figure 10: Performance database for xenon.

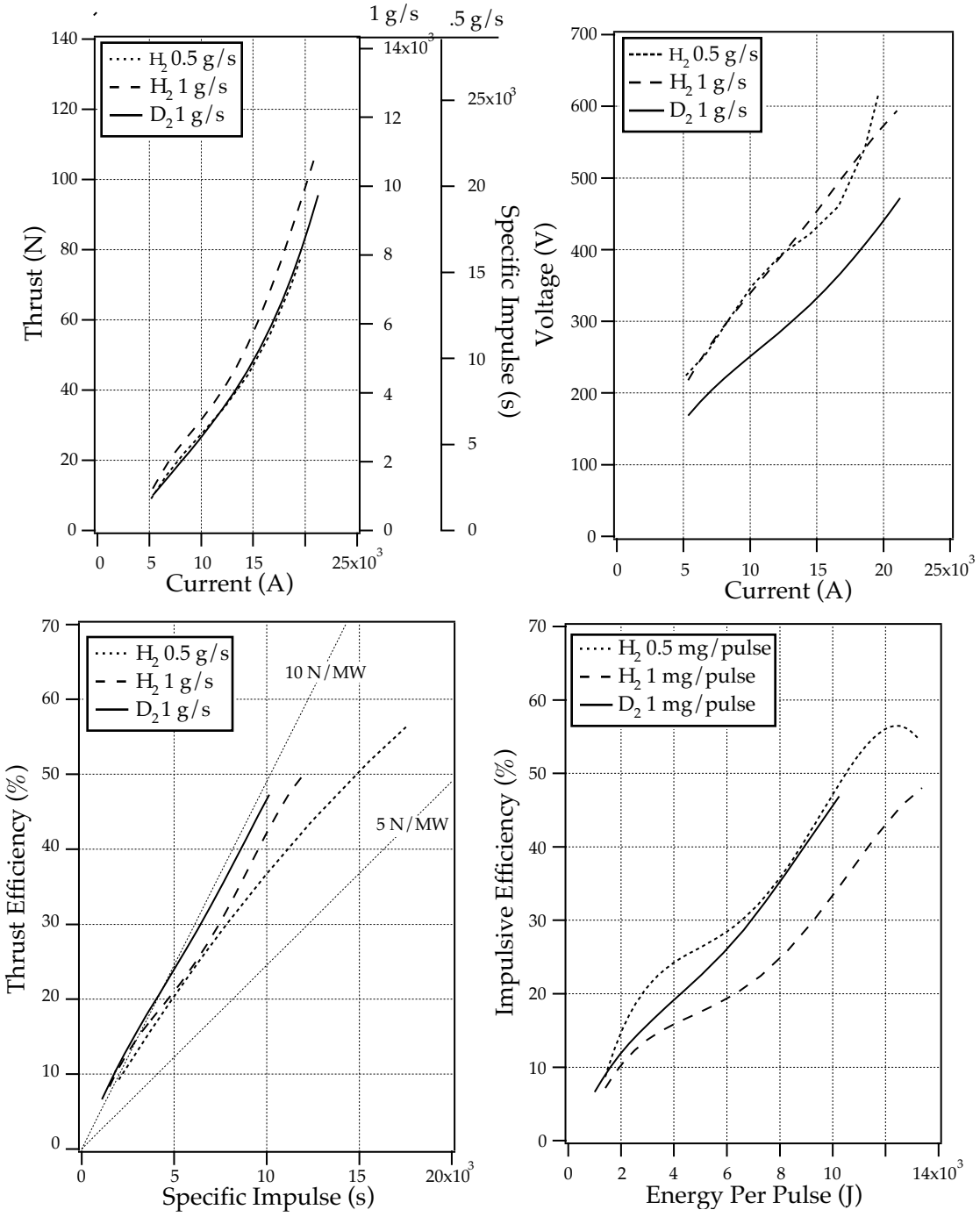

Figure 11: Performance database for hydrogen and deuterium. The corresponding error bars can be obtained from the scatter plots in Fig. (12).

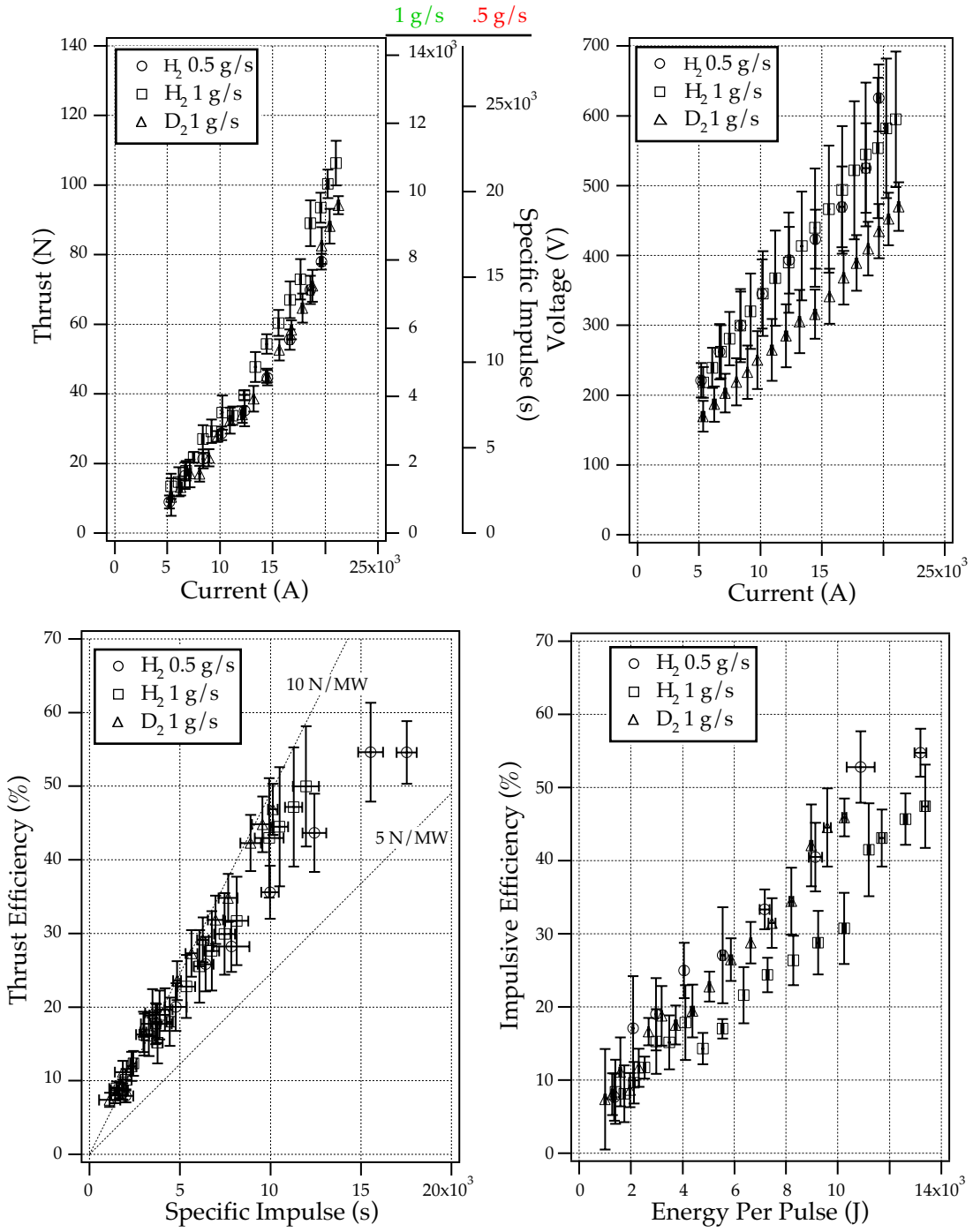

Figure 12: Performance database for hydrogen and deuterium.